

SUBARU SPECTROSCOPY OF THE GLOBULAR CLUSTERS IN THE VIRGO GIANT ELLIPTICAL GALAXY M86*

HONG SOO PARK¹, MYUNG GYOON LEE¹, AND HO SEONG HWANG²

¹ Astronomy Program, Department of Physics and Astronomy, Seoul National University, Seoul 151-742, Republic of Korea;
hspark@astro.snu.ac.kr, mglee@astro.snu.ac.kr

² Smithsonian Astrophysical Observatory, 60 Garden Street, Cambridge, MA 02138, USA; hhwang@cfa.harvard.edu
Received 2012 March 10; accepted 2012 August 6; published 2012 September 17

ABSTRACT

We present the first spectroscopic study of the globular clusters (GCs) in the giant elliptical galaxy (gE) M86 in the Virgo Cluster. Using spectra obtained in the Multi-Object Spectroscopy mode of the Faint Object Camera and Spectrograph on the Subaru telescope, we measure the radial velocities for 25 GCs in M86. The mean velocity of the GCs is derived to be $\bar{v}_p = -354_{-79}^{+81}$ km s⁻¹, which is different from the velocity of the M86 nucleus ($v_{\text{gal}} = -234 \pm 41$ km s⁻¹). We estimate the velocity dispersion of the GCs, $\sigma_p = 292_{-32}^{+32}$ km s⁻¹, and find a hint of rotation in the M86 GC system. A comparison of the observed velocity dispersion profiles of the GCs and stars with a prediction based on the stellar mass profile strongly suggests the existence of an extended dark matter halo in M86. We also estimate the metallicities and ages for 16 and 8 GCs, respectively. The metallicities of M86 GCs are in the range of $-2.0 < [\text{Fe}/\text{H}] < -0.2$ with a mean value of -1.13 ± 0.47 . These GCs show a wide age distribution from 4 to 15 Gyr.

Key words: galaxies: abundances – galaxies: elliptical and lenticular, cD – galaxies: individual (M86, NGC 4406) – galaxies: kinematics and dynamics – galaxies: star clusters: general

Online-only material: color figures

1. INTRODUCTION

Globular clusters (GCs) are excellent tracers for studying the formation history of their host galaxies (Lee 2003; Brodie & Strader 2006). In particular, a giant elliptical galaxy (gE) contains thousands of GCs that range in location from close to the galaxy center to very far away in the outer halo. Therefore, GCs can be used as powerful test particles for studying the kinematics and chemical evolution of gE halos.

There have been several previous kinematic studies of GC systems in nearby gEs: M49 (Zepf et al. 2000; Côté et al. 2003), M60 (Pierce et al. 2006; Bridges et al. 2006; Lee et al. 2008b; Hwang et al. 2008), M87 (Cohen & Ryzhov 1997; Kissler-Patig & Gebhardt 1998; Côté et al. 2001), NGC 4636 (Schuberth et al. 2006; Chakrabarty & Raychaudhury 2008; Park et al. 2010; Lee et al. 2010a), NGC 1399 (Kissler-Patig et al. 1998; Minniti et al. 1998; Kissler-Patig et al. 1999; Richtler et al. 2004, 2008; Schuberth et al. 2010), NGC 5128 (Peng et al. 2004a, 2004b; Woodley et al. 2007), and NGC 1407 (Romanowsky et al. 2009). The data used for these studies were compiled and reanalyzed by Lee et al. (2010a), who found that the kinematic properties of the GC systems are diverse among the gEs, indicating diverse merging and accretion histories of gEs (see also the recent study on the M87 GC system by Strader et al. 2011).

There are also several studies focusing on the spectroscopic ages and metallicities of the gE GCs: Cohen et al. (1998) for M87, Beasley et al. (2000) and Cohen et al. (2003) for M49, Peng et al. (2004b), Beasley et al. (2008), Woodley et al. (2010), and Woodley & Gómez (2010) for NGC 5128, Pierce et al. (2006) for M60, Cenarro et al. (2007) for NGC 1407, and Kissler-Patig et al. (1998) and Forbes et al. (2001) for NGC 1399. Recently, Park et al. (2012) presented a study of spectroscopic ages and metallicities for the GCs in NGC 4636. They also compiled the

data of all the gE GCs in the literature and found that the GC metallicity distribution in the combined gE sample is bimodal.

We have been carrying out a project to investigate the spectroscopic properties of GCs in nearby galaxies in order to understand the formation of GC systems in galaxies. Our study on the kinematics of the GC system of Virgo gE M60 was presented in Lee et al. (2008b) and Hwang et al. (2008) and we presented our study of the GC system of spiral galaxy M31 in Kim et al. (2007) and Lee et al. (2008a). Recently, we presented measurements of the radial velocities for the GCs in NGC 4636 (Park et al. 2010) and a detailed kinematic analysis of these data in Lee et al. (2010a). We also investigated the chemical properties of NGC 4636 GCs and other gE GCs (Park et al. 2012).

Here, we present a spectroscopic study of the GCs in M86 (NGC 4406), a gE in the Virgo Cluster. This galaxy is one of the best targets for the spectroscopic study of the GC system because it is located close to the center of the Virgo Cluster and harbors GCs out to large radii from the galaxy center (Lee et al. 2010b). To date, there has been no published spectroscopic study of M86 GCs.

In contrast to the absence of spectroscopic studies, there have been several studies of the photometric properties of M86 GCs. For example, Kundu & Whitmore (2001) and Larsen et al. (2001) found that the color distribution of M86 GCs is bimodal from an analysis of *Hubble Space Telescope* (HST)/WFPC2 images. This bimodality was confirmed by HST/Advanced Camera for Surveys (ACS) data (Peng et al. 2006) and ground-based wide-field imaging data (Rhode & Zepf 2004; Park 2012). The radial number density profile of the M86 GC system is approximately well fitted by a de Vaucouleurs law and power law (Rhode & Zepf 2004; Park 2012). Basic information about M86 is summarized in Table 1.

This paper is composed as follows. Section 2 describes the spectroscopic target selection, observation, and data reduction. In Section 3, we identify genuine M86 GCs and list the

* Based on data collected with the Subaru telescope, which is operated by the National Astronomical Observatory of Japan.

Table 1
Basic Properties of M86

Galaxy	M_V^a	v_{sys}^b (km s $^{-1}$)	R_{eff}^c (kpc)	ϵ^d	P.A.-min e (deg)	Distance f (Mpc)	σ_{star}^g (km s $^{-1}$)	$\log(L_X)^h$ (erg s $^{-1}$)	N_{GC}^i Blue Red	S_N^j
M86	-22.7	-234	15.36	0.33	29	16.86	259 \pm 28	42.00 \pm 0.002	1453 968	3.5 \pm 0.5

Notes.

- ^a V-band absolute total magnitude: Kormendy et al. (2009).
^b Systemic velocity: this study.
^c Effective radius in R band: Park (2012).
^d Ellipticity at R_{eff} : Park (2012).
^e Position angle of the minor axis at R_{eff} : Park (2012).
^f Distance: Mei et al. (2007).
^g Mean velocity stellar dispersion at $R \lesssim 45''$: Bender et al. (1994).
^h Logarithmic value of X-ray luminosity: Beuing et al. (1999).
ⁱ Numbers of blue GCs and red GCs: Rhode & Zepf (2004).
^j Specific frequency of GCs: Rhode & Zepf (2004).

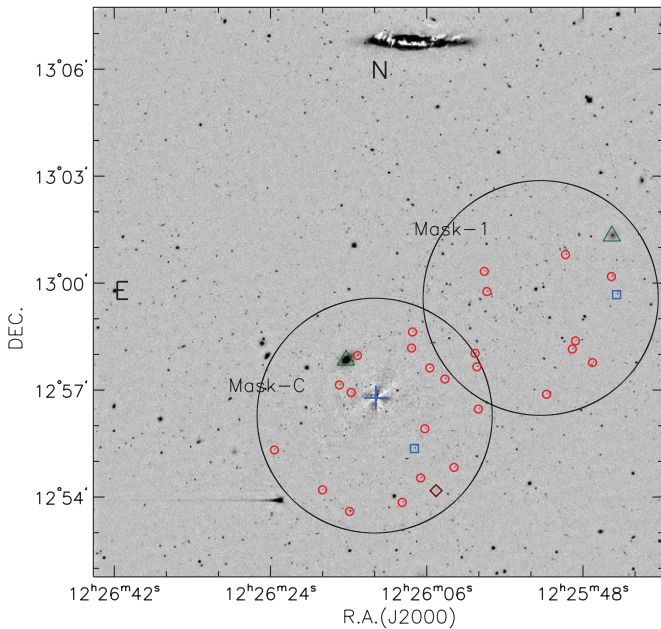


Figure 1. Gray-scale map of the T_1 image of M86 taken with the KPNO 4 m telescope. The M86 stellar light is subtracted from the original image to highlight the point sources. The large circles and plus sign indicate the observed masks and the center of M86, respectively. The small circles, diamond, triangles, and squares represent the GCs in M86, a probable intracluster GC in the Virgo Cluster, background galaxies, and foreground stars, respectively. (A color version of this figure is available in the online journal.)

corresponding photometric and spectroscopic data. We present the kinematic properties of the M86 GC system in Section 4, and the metallicities and ages of the M86 GCs in Section 5. The primary results are summarized in the final section.

2. OBSERVATIONS AND DATA REDUCTION

2.1. Spectroscopic Target Selection

We selected the spectroscopic targets from a photometric sample of the GC candidates in M86 identified in Washington CT_1 images ($15'.8 \times 15'.8$) taken at the KPNO 4 m telescope (Park 2012). The GCs in M86 appear as point sources in the ground-based KPNO images, and we first selected point sources around M86 with colors of $0.9 < (C - T_1) < 2.1$ as GC candidates. This $(C - T_1)$ color selection criterion is effective in selecting GC candidates in early-type galaxies: the success rate of the

Table 2
Observing Log for the Subaru FOCAS/MOS Run

Mask Name	R.A. (J2000)	Decl. (J2000)	N (objects)	T (exp) (s)	Seeing ($''$)	Date (UT)
Mask-C	12:26:11.7	12:56:17	34	3 \times 1200	0.6	2002 Apr 21
Mask-1	12:25:52.3	12:59:39	33	1 \times 1800	0.6	2002 Apr 21

photometric search for GCs is about 90% in the case of M87 (Côté et al. 2001), M49 (Côté et al. 2003), and NGC 4636 (Park et al. 2010). We then selected from the bright sources with magnitudes $19 < T_1 < 21.5$ as the spectroscopic targets. A total of 67 targets were chosen, which included the M86 nucleus and two known faint galaxies (NGC 4406B, VCC 0833). We also observed two red, bright point sources with $(C - T_1) \sim 3$ to fill the mask gaps.

2.2. Observations

We obtained spectra of the 67 targets from observations in the Multi-Object Spectroscopy (MOS) mode of the Faint Object Camera and Spectrograph (FOCAS; Kashikawa et al. 2002) at the Subaru 8.2 m telescope on 2002 April 21. We observed two circular masks with diameters of $6'$. Figure 1 presents a gray-scale map of the T_1 image of M86 taken at the KPNO 4 m telescope, which shows the positions of the spectroscopic targets as well as the observed masks. We subtracted the M86 stellar light from the original image using the IRAF/ELLIPSE³ task to show the point sources clearly.

The observational log is given in Table 2. We used a medium-dispersion blue grism (300B) with a dispersion of $1.34 \text{ \AA pixel}^{-1}$ and an order-cut filter L600 covering $3700\text{--}6000 \text{ \AA}$. Seeing during the observation was $0''.6$. To make the masks, we obtained R-band pre-images with exposure times of 180 s in the FOCAS camera mode under a seeing condition of $\sim 1''.0$ on 2002 March 9. Using these images, we constructed masks with Mask Design Pipeline, a software utility for MOS (Saito et al. 2003). The slit width along the dispersion axis was $0''.8$, and the resulting spectral resolution was $R \sim 500$.

We used three 1200 s exposures in mask-C and one 1800 s exposure in mask-1. We also obtained the comparison spectra with Th-Ar lamps before and/or after each exposure. We used

³ IRAF is distributed by the National Optical Astronomy Observatory, which is operated by the Association of Universities for Research in Astronomy, Inc., under contract with the National Science Foundation.

the FOCAS long-slit spectroscopy mode to calibrate the flux, radial velocity, and metallicity. We observed a standard star, BD+33d2642, for the flux calibration and five Milky Way (MW) GCs (M5, M13, M92, M107, and NGC 6624) for the velocity and metallicity calibrations. We observed the MW GCs with stepping scan mode by moving the slit along the dispersion direction to sample an area larger than that covered by the slit. We observed these calibration targets during the same run and also used their spectra in the study of the NGC 4636 GCs (Park et al. 2010). Details of the long-slit mode observation are given in Section 2.2 and Table 2 of Park et al. (2010).

2.3. Data Reduction

We first applied basic processing techniques (overscan correction, bias subtraction, and cosmic-ray rejection) to the CCD images using IRAF tasks; the CCD images were obtained with a pair of $4K \times 2K$ CCDs. We used the *FOCASRED/bigimage* task in IDL (Saito et al. 2003) to produce a large single image from a pair of CCD images and correct distortions in the optics. We then clipped the two-dimensional spectrum of each target out of the single image and applied a flat-field correction. The spectrum from each two-dimensional image was traced, extracted, and sky-subtracted using the IRAF/APALL task. We could not extract the spectra of seven faint targets because of a low signal-to-noise ratio (S/N). Wavelength calibration was performed using Th–Ar lamp spectra with ~ 40 useful emission lines in the 3800–6000 Å range. The typical rms error for this calibration is ~ 0.8 Å. The flux of the target spectra was calibrated using the flux standard star.

Sample flux-calibrated spectra of an M86 GC, a foreground star, and the M86 nucleus are shown in Figure 2. We classified the target (ID 81) in panel (b) as a K2III star because of the broad (~ 300 Å) absorption feature around the Mgb index. This feature is typically seen in the K giant star templates (Santos et al. 2002) but not in GC templates. Several absorption lines typically seen in old stellar systems including the *G* band, $H\beta$, and Mgb are clearly visible in the M86 GC spectrum in panel (a). Absorption features in the spectrum of the M86 nucleus are much broader than those in the GC and star because of its large velocity dispersion.

3. MEMBERSHIP DETERMINATION

3.1. Velocity Measurement

We measured the radial velocities for the targets using the Fourier cross-correlation task, IRAF/FXCOR (Tonry & Davis 1979). A wavelength range of 4200–5400 Å was used for the cross-correlation because of the low S/N at ~ 4000 Å and the strong night sky emission line [O I] at 5577 Å. During the cross-correlation, we fit the continuum of the spectra using a spline function with a 2σ clipping for the low level and a 4σ clipping for the high level. Radial velocities were measured for each target using the five MW GC templates; velocities for M86 GCs derived from the M5, M13, M92, and NGC 6624 templates are consistent within 1σ , but those from the M107 template differ by 2σ . Therefore, an error-weighted average of the first four measurements was taken to give the final radial velocity for each target. The error in the measured radial velocity is estimated as $\langle \epsilon_v \rangle = (\sum \epsilon_i^{-2})^{-1/2}$, where ϵ_i is the error in each measurement.

The final number of targets with measured radial velocities is 31. The radial velocities for 36 objects among the original 67 could not be determined because of the poor quality of the spectra. We determined the radial velocity of the M86 nucleus to

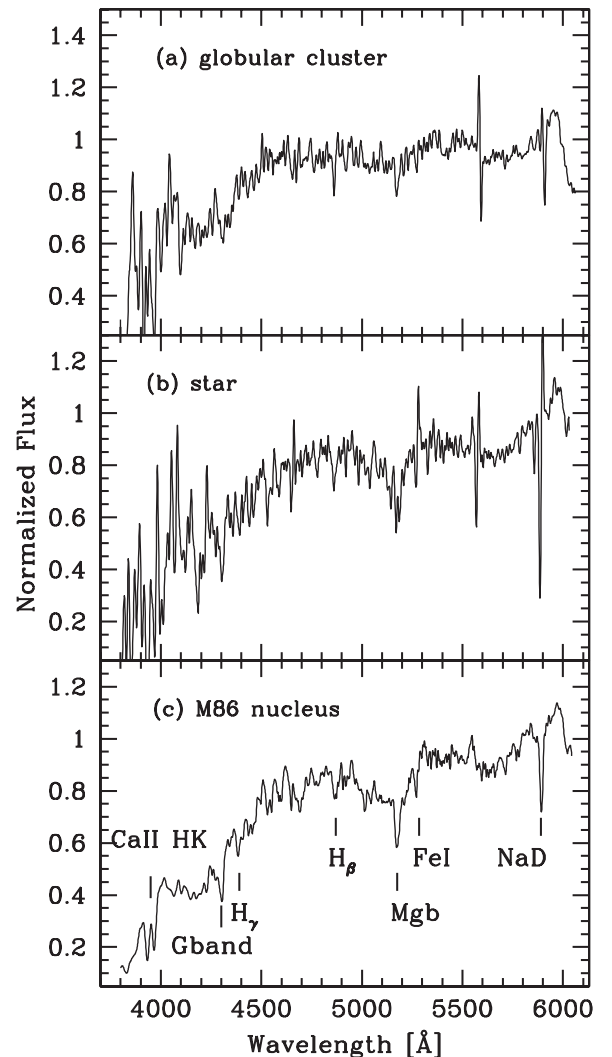


Figure 2. Sample spectra: (a) a GC in M86 (ID = 65) with $T_1 = 19.72$ mag, $(C - T_1) = 1.49$, and $[\text{Fe}/\text{H}] = -0.98$ dex, (b) a star (ID=81) with $T_1 = 19.89$ mag classified as a K2III red giant star, and (c) the M86 nucleus. All spectra are plotted in the rest frame, smoothed using a boxcar filter with 6.7 Å, and normalized at 5870 Å.

be $v_p = -234 \pm 41$ km s^{-1} , which is consistent with the previous measurement $v_p = -244 \pm 5$ km s^{-1} (Smith et al. 2000). We also measured the radial velocities for two faint galaxies: $v_p = 777 \pm 38$ km s^{-1} for VCC 0833 and $v_p = 949 \pm 23$ km s^{-1} for NGC 4406B. These values are also consistent with previous measurements (Sloan Digital Sky Survey and Strauss et al. 1992). Errors in our velocity measurements range from 20 to 90 km s^{-1} with a mean error of 49 ± 16 km s^{-1} .

3.2. Membership Determination

To identify genuine M86 GCs among the 31 objects with measured velocities, we used $(C - T_1)$ colors and radial velocities. The $(C - T_1)$ colors are plotted as a function of the radial velocity in Figure 3; note that the M86 nucleus and two faint galaxies are not included in the plot. The velocity distribution in panel (b) shows that all objects have velocities of -900 to $+300$ km s^{-1} except for one object with a very large velocity of $v_p \sim 2400$ km s^{-1} . We consider the objects with -900 km $s^{-1} < v_p < 300$ km s^{-1} and $0.9 \leq (C - T_1) < 2.1$ to be genuine GCs bound to M86 (the velocity of the M86 nucleus is -234 km s^{-1}).

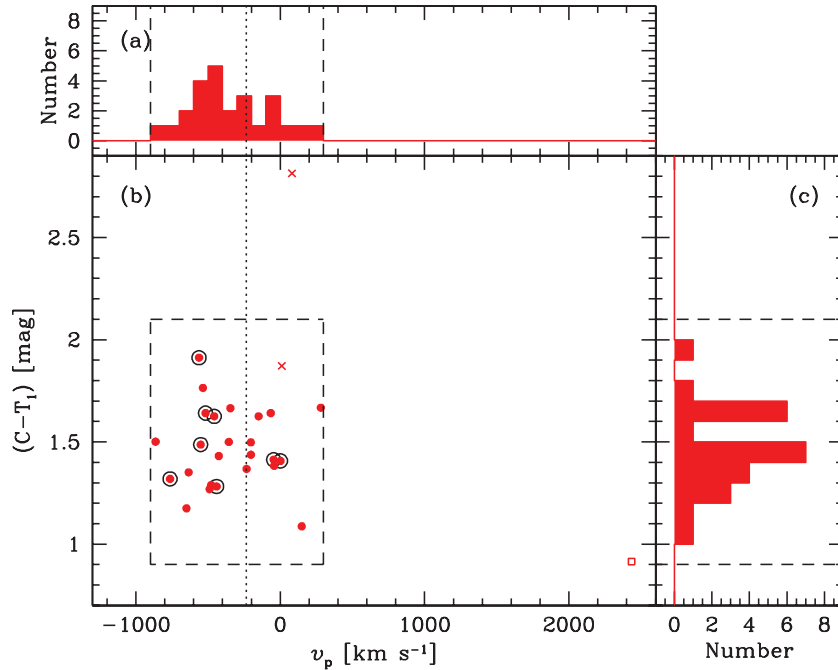


Figure 3. $(C - T_1)$ color as a function of the radial velocity of the M86 GCs: (a) radial velocity distribution, (b) $(C - T_1)$ vs. radial velocity, and (c) $(C - T_1)$ distribution. The circles, crosses, and square represent the M86 GCs, foreground stars, and a probable intracluster GC, respectively. The open circles indicate the GCs included in the ACSVCS catalog. The box indicated by the dashed line represents the boundary for selecting the M86 GCs. The vertical dotted line indicates the radial velocity of the M86 nucleus.

(A color version of this figure is available in the online journal.)

The $(C - T_1)$ color range is equivalent to a metallicity range of $-2.24 \text{ dex} \lesssim [\text{Fe}/\text{H}] \lesssim 0.33 \text{ dex}$ (Lee et al. 2008c).

Among the 28 objects (excluding the M86 nucleus and two faint galaxies), two do not satisfy the GC selection criteria. One target (ID 226) is classified as a star because its color is too red, $(C - T_1) > 2.1$, even though it satisfies the velocity criterion. The other target (ID 446) satisfies the color criterion but does not satisfy the velocity criterion: $v_p = 2434 \pm 52 \text{ km s}^{-1}$. This object seems to be an intracluster GC in the Virgo Cluster.

Because the systemic velocity of M86 is similar to the radial velocities of the MW stars, there could be some MW stars that satisfy our GC selection criteria. To remove these stars, we performed a careful visual inspection of the target spectra. We found one object (ID 81) with stellar spectral features (see Section 2.3 and Figure 2(b)) and rejected it from the M86 GC catalog. Thus, 25 genuine M86 GCs out of 28 targets, excluding the M86 nucleus and two faint galaxies, were identified. We note that there may be one or two more stars among the 25 GCs considering the selection efficiency for the GC candidates (see Section 2.1).

The reliability of our M86 GCs was further checked against the ACS Virgo Cluster Survey (ACSVCS) source catalog (Jordán et al. 2009). This catalog provides the classification probability for GC candidates in 100 Virgo early-type galaxies. We found that eight GCs (ID = 448, 284, 65, 270, 316, 107, 430, and 324) among the 25 M86 GCs are included in the ACSVCS catalog, and all of the eight have a GC probability larger than 90%, which confirms our classification. We show these eight GCs as open circles in Figure 3.

3.3. A Catalog of the M86 GCs

Table 3 lists the photometric and spectroscopic data including the metallicities of 16 GCs using the BH (Brodie & Huchra

method and the ages and metallicities of eight GCs using the grid method (see Section 5). The first column represents the identification number. The second and third columns give the right ascension and declination (J2000), respectively. The galactocentric radius and position angle (P.A.) are given in Columns 4 and 5, respectively. The magnitude and color information in Columns 6 and 7 are from Park (2012). Column 8 gives the radial velocity and its error measured in this study. Columns 9 and 10 give the age and metallicity derived from the grid method. Column 11 gives the metallicity derived from the BH method. The final column indicates the corresponding mask from Table 2. The M86 GCs are listed first, followed by foreground stars, a probable intracluster GC, and the faint galaxies and M86 nucleus.

4. KINEMATICS

4.1. Mean Velocities and Velocity Dispersions of M86 GCs

The M86 GCs in our sample are found in a radial range of $42''\text{--}446''$ (i.e., 3.4–36.1 kpc, see Figure 1). The mean radial velocity for the 25 GCs determined with the biweight location of Beers et al. (1990) is $\bar{v}_p = -354_{-79}^{+81} \text{ km s}^{-1}$, which is smaller than the radial velocity for the M86 nucleus ($v_{\text{gal}} = -234 \pm 41 \text{ km s}^{-1}$). The radial velocity distribution for the M86 GCs is shown in the top panel of Figure 4; the distribution appears to be Gaussian. The I statistics (Teague et al. 1990) gave an I value of 1.022, which is smaller than the critical value for rejecting the Gaussian hypothesis at the 90% confidence level, $I_{0.90} = 1.176$. This suggests that the velocity distribution of the M86 GCs follows a Gaussian distribution. A Gaussian fit yields a peak at $v_p = -343 \text{ km s}^{-1}$ with a width of $\sigma_p = 279 \text{ km s}^{-1}$.

The bottom panel of Figure 4 shows the radial velocities as a function of the projected galactocentric radius R . Mean

Table 3
Radial Velocity, Age, and Metallicity of Globular Clusters in M86

ID ^a	R.A. (J2000)	Decl. (J2000)	R (arcsec)	Θ (deg)	T_1 (mag)	$(C - T_1)$ (mag)	v_p (km s ⁻¹)	Age (Gyr)	[Z/H] (dex)	[Fe/H] _{BH} (dex)	Mask
Globular Clusters											
448	12:26:07.53	12:58:37.6	127.1	331.0	21.31 ± 0.02	1.41 ± 0.03	2 ± 51	C
284	12:26:07.63	12:58:10.4	103.3	324.4	20.88 ± 0.02	1.28 ± 0.02	-441 ± 59	-1.26 ± 0.29	C
65	12:26:13.87	12:57:57.7	77.7	23.5	19.72 ± 0.01	1.49 ± 0.02	-551 ± 24	7.3 ± 2.4	-0.89 ± 0.18	-0.98 ± 0.25	C
270	12:26:05.54	12:57:36.8	103.8	299.0	20.84 ± 0.01	1.41 ± 0.02	-46 ± 47	4.5 ± 3.6	-0.50 ± 0.34	-1.07 ± 0.23	C
316	12:26:03.79	12:57:18.1	120.6	285.3	20.98 ± 0.01	1.32 ± 0.02	-763 ± 64	C
107	12:26:15.94	12:57:08.0	65.0	70.6	20.09 ± 0.01	1.64 ± 0.02	-517 ± 26	6.6 ± 3.8	-0.35 ± 0.21	-0.44 ± 0.26	C
430	12:26:14.59	12:56:55.3	42.4	77.9	21.31 ± 0.02	1.91 ± 0.05	-563 ± 51	C
265	12:25:59.94	12:56:27.6	173.6	263.8	20.82 ± 0.02	1.38 ± 0.03	-42 ± 43	-1.28 ± 0.20	C
324	12:26:06.09	12:55:54.4	97.7	237.8	21.02 ± 0.02	1.62 ± 0.04	-457 ± 36	C
289	12:26:02.72	12:54:49.3	176.4	228.4	20.91 ± 0.01	1.76 ± 0.03	-536 ± 71	C
332	12:26:06.58	12:54:31.5	154.6	209.3	21.05 ± 0.01	1.37 ± 0.03	-233 ± 45	-1.91 ± 0.29	C
143	12:26:08.69	12:53:50.4	181.6	194.2	20.31 ± 0.02	1.62 ± 0.03	-150 ± 33	14.9 ± 4.0	0.06 ± 0.12	-0.39 ± 0.37	C
77	12:26:14.73	12:53:35.2	196.2	167.1	19.85 ± 0.01	1.67 ± 0.02	282 ± 36	-0.25 ± 0.32	C
413	12:26:23.40	12:55:18.5	191.7	117.3	21.26 ± 0.02	1.66 ± 0.03	-345 ± 53	C
299	12:26:17.86	12:54:11.4	178.9	150.0	20.93 ± 0.01	1.64 ± 0.03	-66 ± 32	-1.11 ± 0.41	C
58	12:25:49.93	13:00:48.0	399.9	307.2	19.66 ± 0.01	1.50 ± 0.01	-356 ± 36	12.0 ± 1.9	-1.26 ± 0.10	-0.97 ± 0.13	1
79	12:25:44.66	13:00:11.0	445.6	297.3	19.86 ± 0.02	1.50 ± 0.03	-864 ± 57	14.4 ± 4.7	-0.98 ± 0.19	-1.29 ± 0.25	1
302	12:25:48.78	12:58:22.6	349.3	286.0	20.93 ± 0.01	1.35 ± 0.02	-635 ± 70	1
96	12:25:49.15	12:58:08.9	340.5	284.0	20.00 ± 0.01	1.09 ± 0.03	149 ± 49	6.2 ± 2.0	-0.76 ± 0.17	-1.67 ± 0.66	1
251	12:25:46.82	12:57:46.1	369.2	279.3	20.78 ± 0.02	1.50 ± 0.04	-204 ± 49	1
352	12:25:52.11	12:56:52.7	287.2	271.3	21.10 ± 0.01	1.43 ± 0.04	-426 ± 52	-1.09 ± 0.34	1
258	12:25:59.27	13:00:19.8	280.7	319.5	20.79 ± 0.03	1.27 ± 0.04	-490 ± 93	1
142	12:25:58.97	12:59:45.7	258.9	313.8	20.30 ± 0.02	1.44 ± 0.03	-203 ± 77	-1.14 ± 0.53	1
149	12:26:00.32	12:58:01.6	183.2	294.2	20.34 ± 0.01	1.18 ± 0.02	-649 ± 43	12.0 ± 0.1	-1.10 ± 0.16	-1.45 ± 0.35	1
150	12:26:00.13	12:57:38.8	177.8	287.1	20.34 ± 0.01	1.29 ± 0.02	-479 ± 47	-1.76 ± 0.31	1
Stars											
81	12:26:07.30	12:55:21.1	107.3	217.3	19.89 ± 0.02	1.87 ± 0.03	10 ± 27	C
226	12:25:44.08	12:59:40.6	440.3	293.3	20.73 ± 0.01	2.81 ± 0.04	81 ± 44	1
Probable Intracluster Globular Cluster in the Virgo Cluster											
446	12:26:04.79	12:54:10.2	186.4	213.1	21.30 ± 0.03	0.91 ± 0.04	2434 ± 52	C
Galaxies											
VCC 0833	12:25:44.63	13:01:19.3	481.2	304.5	777 ± 38	14.0 ± 0.0	-0.64 ± 0.09	-0.90 ± 0.31	1
NGC 4406B	12:26:15.18	12:57:49.8	80.9	38.4	949 ± 23	14.0 ± 0.1	-0.58 ± 0.12	-1.12 ± 0.39	C
M86	12:26:11.74	12:56:46.4	0.0	0.0	-234 ± 41	4.0 ± 0.3	0.26 ± 0.02	0.62 ± 0.46	C

Note. ^a From Park (2012).

velocities of the GCs in the inner ($42'' \leq R < 240''$) and outer ($240'' \leq R < 446''$) regions are similar to that of the GCs in the entire region. The velocity difference between the GC samples and the M86 nucleus is more visible in this panel.

The velocity dispersion of the M86 GCs determined with the biweight scale of Beers et al. (1990) is $\sigma_p = 292_{-32}^{+32}$ km s⁻¹. The velocity dispersion of the GCs in the inner region, $\sigma_p = 292_{-39}^{+39}$ km s⁻¹, is similar to that in the outer region, $\sigma_p = 314_{-90}^{+90}$ km s⁻¹. It is noted that the velocity dispersion determined in this study could be contaminated by the inclusion of possible MW stars because the systemic velocity of M86, $v_{\text{gal}} = -234$ km s⁻¹, is in the velocity range of the MW stars.

The plot of the radial velocities as a function of the $(C - T_1)$ colors, T_1 magnitudes, and P.A.s Θ (measured from the north to east) in Figure 5 shows that the mean values of the radial velocities do not change with either the magnitude or the color. However, the mean values of the radial velocities seem to depend on the P.A., showing a minimum value at $\Theta \approx 60^\circ$ and $\approx 300^\circ$. This suggests a rotation of the M86 GC system (discussed in detail in the next section).

4.2. Rotation of the GC System

In Figure 6, we show the spatial distribution of the M86 GCs with measured velocities. Although the spatial coverage is neither uniform nor large, the spatial segregation of the high-velocity and low-velocity GCs relative to the velocity of the M86 nucleus can be seen, which indicates a rotation of the GC system (see also Figure 5(c)).

The amplitude and axis of rotation for the M86 GC system was measured with the following assumptions: (1) the GC system is spherically symmetric and (2) the rotation axis of the GC system lies in the plane of the sky. If the GCs follow any overall rotation, the radial velocities will depend sinusoidally on the azimuthal angles. Thus, we can then determine the amplitude and axis of rotation by fitting the radial velocities (v_p) to the function (Côté et al. 2001, 2003; Hwang et al. 2008; Lee et al. 2010a),

$$v_p(\Theta) = v_{\text{sys}} + (\Omega R) \sin(\Theta - \Theta_0), \quad (1)$$

where ΩR is the rotation amplitude and v_{sys} is the systemic velocity of the GC system.

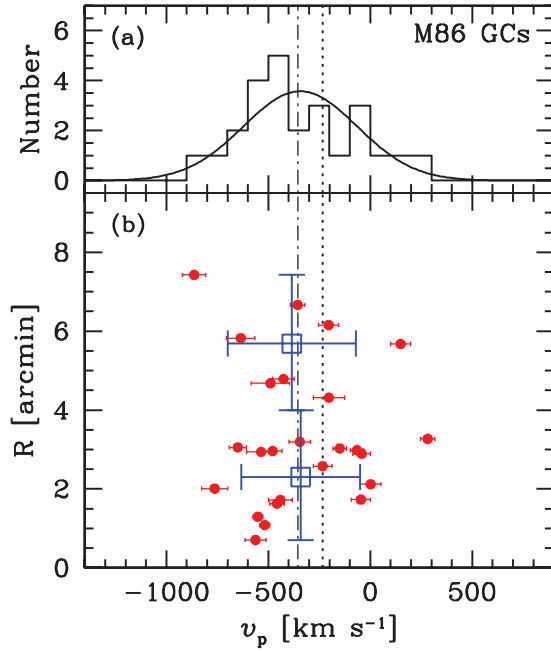


Figure 4. (a) Radial velocity distribution and (b) projected galactocentric radii vs. radial velocities for the M86 GCs. The large open squares represent the mean radial velocities of the GCs in each radial bin represented by the long vertical error bars. The horizontal error bars denote the velocity dispersions in each radial bin. The vertical dot-dashed and dotted lines indicate the mean velocity and velocity of the M86 nucleus, respectively. The solid curved line in (a) is a Gaussian fit of the data.

(A color version of this figure is available in the online journal.)

Figure 7 plots the radial velocities of the GCs as a function of the P.A. and an overlay of the best-fit rotation curve. We use an error-weighted, nonlinear fit of Equation (1) with v_{sys} fixed to the value of the M86 nucleus velocity. This gives a rotation amplitude of $\Omega R = 228^{+71}_{-80}$ km s⁻¹, which suggests a rotation of the M86 GC system. However, as this result is based on a small sample size, it will need to be examined again with a larger number of GCs in future studies.

The orientation of the rotation axis (Θ_0) is estimated to be 91^{+19}_{-21} , and this appears to be closer to the photometric major axis of M86 ($\Theta_{\text{phot}} = 120^\circ$) than to the minor axis. The rotation of the M86 GC system around the major axis is consistent with the result based on stellar kinematics, although the spatial coverage of the stellar kinematics was much smaller than this study (Krajinović et al. 2011).

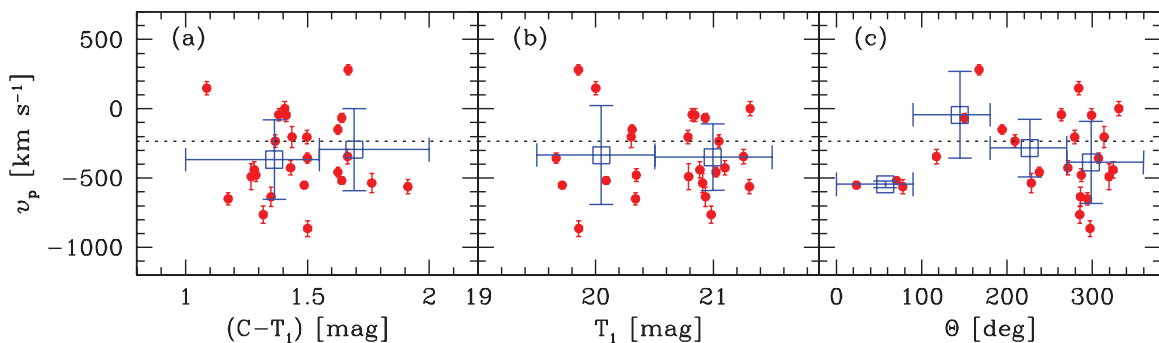


Figure 5. Radial velocities as a function of (a) $(C - T_1)$ color, (b) T_1 magnitude, and (c) position angle, Θ , for the M86 GCs. The large open squares indicate the mean radial velocities of the GCs in each bin, represented by a long horizontal error bar. The vertical error bars denote the velocity dispersions of the GCs in the radial bins. The horizontal dotted line indicates the radial velocity of the M86 nucleus.

(A color version of this figure is available in the online journal.)

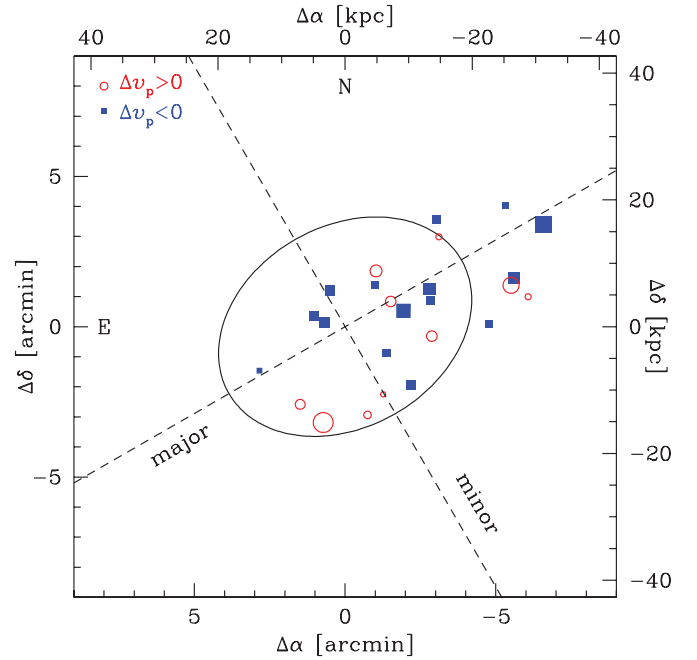


Figure 6. Spatial distribution of the 25 identified M86 GCs. GCs with velocities larger and smaller than the velocity of the M86 nucleus are plotted with open circles and filled boxes, respectively. The solid ellipse represents the boundary for the standard major diameter D_{25} of M86 (de Vaucouleurs et al. 1991). The dashed lines represent the photometric major and minor axes.

(A color version of this figure is available in the online journal.)

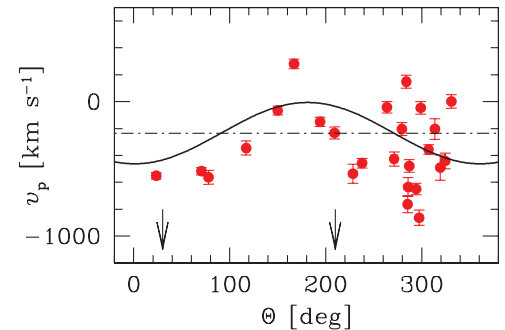


Figure 7. Radial velocity vs. position angle of the M86 GCs. The solid curve is a best-fit rotation curve from Table 4. The horizontal dot-dashed line represents the velocity of the M86 nucleus. The vertical arrows show the photometric minor axis of M86.

(A color version of this figure is available in the online journal.)

Table 4
Kinematics of the M86 Globular Cluster System

R (arcsec)	$\langle R \rangle$ (arcsec)	N	$\overline{v_p}$ (km s $^{-1}$)	σ_p (km s $^{-1}$)	Θ_0 (deg)	ΩR (km s $^{-1}$)	$\sigma_{p,r}$ (km s $^{-1}$)	$\Omega R/\sigma_{p,r}$
42–446	203	25	-354^{+81}_{-79}	292^{+32}_{-32}	91^{+19}_{-21}	228^{+71}_{-80}	282^{+36}_{-33}	$0.81^{+0.32}_{-0.30}$

We summarize the kinematic results of the M86 GC system in Table 4: the range of the galactocentric radius of the GCs in arcseconds, the mean value of the radial distance in arcseconds, the number of GCs, the mean projected velocity and velocity dispersion about the mean velocity (σ_p), the P.A. of the rotation axis and rotation amplitude estimated using Equation (1), the velocity dispersion about the best-fit rotation curve ($\sigma_{p,r}$), and the absolute value of the ratio of the rotation amplitude to the velocity dispersion about the best-fit rotation curve. The uncertainties of the values represent 68% (1σ) confidence intervals that were determined from the numerical bootstrap procedure following the method of Côté et al. (2001).

4.3. Existence of Dark Matter Halo

Here, we investigate the existence of an extended dark matter halo in M86 by comparing the observed velocity dispersion profile (VDP) of the GCs with the VDP expected from the stellar mass profile (Côté et al. 2001, 2003; Hwang et al. 2008; Lee et al. 2010a). The stellar mass profile is derived from the surface brightness profile of M86, which is then used to compute the VDP.

Assuming that the M86 GC system is spherically symmetric in the absence of rotation, we apply the spherical Jeans equation (e.g., Binney & Tremaine 1987) to a dynamical analysis of the GC system. The spherical Jeans equation is

$$\frac{d}{dr} n_{\text{cl}}(r) \sigma_r^2(r) + \frac{2\beta_{\text{cl}}(r)}{r} n_{\text{cl}}(r) \sigma_r^2(r) = -n_{\text{cl}}(r) \frac{GM_{\text{tot}}(r)}{r^2}, \quad (2)$$

where r is the three-dimensional radial distance from the galactic center, $n_{\text{cl}}(r)$ is the three-dimensional density profile of the GC system, $\sigma_r(r)$ is the radial component of velocity dispersion, $\beta_{\text{cl}}(r) \equiv 1 - \sigma_\theta^2(r)/\sigma_r^2(r)$ is the velocity anisotropy, G is the gravitational constant, and $M_{\text{tot}}(r)$ is the total gravitating mass contained within a sphere of radius r . The tangential component of velocity dispersion, $\sigma_\theta(r)$, is equal to the azimuthal component of the velocity dispersion, $\sigma_\phi(r)$, in the absence of rotation. The total mass $M_{\text{tot}}(r)$ interior out to any radius is the sum of the dark matter mass $M_{\text{dm}}(r)$ and stellar mass $M_s(r)$.

To solve Equation (2), $n_{\text{cl}}(r)$ and $M_s(r)$ are obtained from the observation. If we fix $\beta_{\text{cl}}(r)$ as a constant and assume $M_{\text{dm}}(r)$, we can predict the profile of $\sigma_r(r)$. A comparison of this with the observed VDP will provide information about the existence of a dark matter halo. Because the observed VDP for the GCs is projected, we also need to compute the projected VDP, $\sigma_p(R)$:

$$\sigma_p^2(R) = \frac{2}{N_{\text{cl}}(R)} \int_R^\infty n_{\text{cl}} \sigma_r^2(r) \left(1 - \beta_{\text{cl}} \frac{R^2}{r^2}\right) \frac{r dr}{\sqrt{r^2 - R^2}}, \quad (3)$$

where R is the projected galactocentric distance and the surface density profile, $N_{\text{cl}}(R)$, is the projection of the three-dimensional density profile $n_{\text{cl}}(r)$.

4.3.1. Density Profile of the M86 GC System

The three-dimensional density profiles are derived from the surface number density of the M86 GCs using the

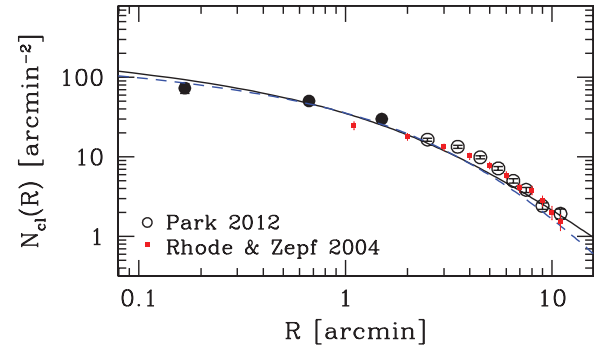


Figure 8. Projected surface number density profile for the M86 GCs. The filled and open circles represent the GC candidates from the *HST*/ACS images and those from the KPNO CT_1 images, respectively (Park 2012). The small squares represent the results from Rhode & Zepf (2004). The solid and dashed lines indicate the projected best fits using the NFW and Dehnen density profiles, respectively.

(A color version of this figure is available in the online journal.)

Navarro–Frenk–White (NFW) profile (Navarro et al. 1997) and the Dehnen profile (Dehnen 1993). We adopt the surface density profile given in Park (2012), which was derived using data from the *HST*/ACSVCS (Jordán et al. 2009) for GCs at $R < 2''$ and from the KPNO CT_1 data for GCs at $R > 2''$. The surface number density profile $N_{\text{cl}}(R)$ is shown in Figure 8. We fit the surface number density profile to the projections of the NFW profile, $n_{\text{cl}}(r) = n_0(r/b)^{-1}(1+r/b)^{-2}$ and the Dehnen profile, $n_{\text{cl}}(r) = n_0(r/a)^{-\Gamma}(1+r/a)^{\Gamma-4}$. The profile $N_{\text{cl}}(R)$ is derived from an integration of the three-dimensional density profile $n_{\text{cl}}(r)$ as follows:

$$N_{\text{cl}}(R) = 2 \int_R^\infty n_{\text{cl}}(r) \frac{r dr}{\sqrt{r^2 - R^2}}. \quad (4)$$

The results of the fit are summarized as follows:

$$\begin{aligned} n_{\text{cl}}^{\text{NFW}}(r) &= 0.052 \text{ kpc}^{-3} (r/14.58 \text{ kpc})^{-1} (1+r/14.58 \text{ kpc})^{-2} \\ n_{\text{cl}}^{\text{Dehnen}}(r) &= 0.028 \text{ kpc}^{-3} (r/27.94 \text{ kpc})^{-0.93} (1+r/27.94 \text{ kpc})^{-3.07}. \end{aligned} \quad (5)$$

4.3.2. Stellar Mass Profile

Figure 9 gives the radial profile of the M86 surface brightness, derived from the KPNO R -band images (Park 2012), and stellar mass. This surface brightness profile agrees well with the results in Peletier et al. (1990), which are based on R -band photometry, and with those in Caon et al. (1990), which are converted from B -band photometry.

A fit of the surface brightness profile of Park (2012) to the projection of the three-dimensional luminosity density profile (Côté et al. 2003; Hwang et al. 2008; Lee et al. 2010a) represented by

$$j(r) = \frac{(3-\gamma)(7-2\gamma)}{4} \frac{L_{\text{tot}}}{\pi a^3} \left(\frac{r}{a}\right)^{-\gamma} \left[1 + \left(\frac{r}{a}\right)^{1/2}\right]^{2(\gamma-4)} \quad (6)$$

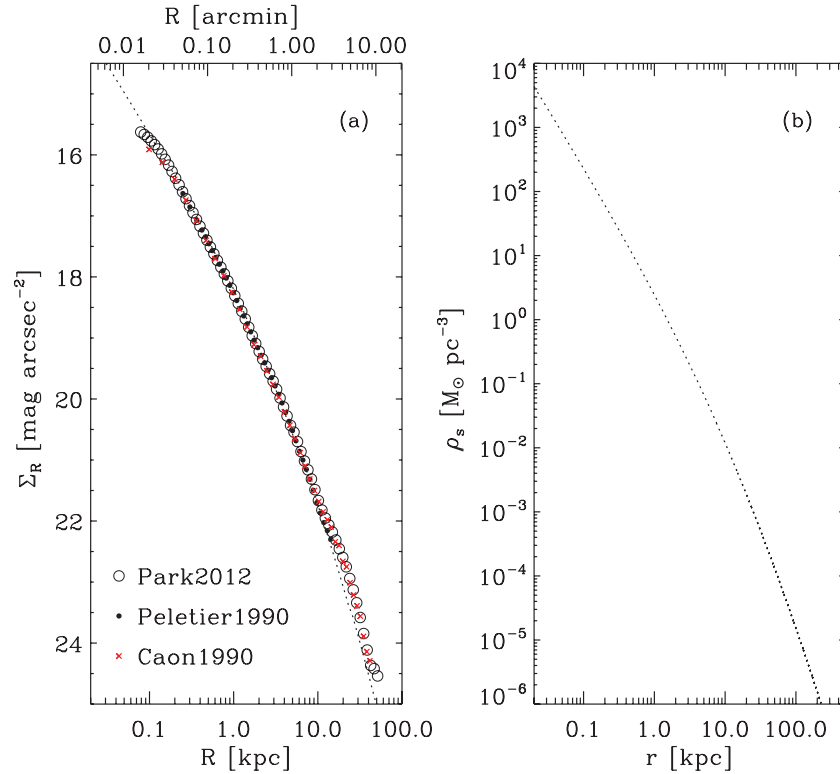


Figure 9. (a) Surface brightness profiles of M86. The open and filled circles are R -band surface photometry given in Park (2012) and in Peletier et al. (1990), respectively. The crosses represent the surface photometry converted from B -band photometry given in Caon et al. (1990). The dotted line represents a projected best fit of the three-dimensional luminosity density profile. (b) Three-dimensional stellar mass density profile derived with a constant R -band mass-to-light ratio of $\Upsilon_0 = 6.5 M_\odot L_{R,\odot}^{-1}$.

(A color version of this figure is available in the online journal.)

gives $\gamma = 1.75$, $L_{\text{tot}} = 1.60 \times 10^{11} L_{R,\odot}$, and $a = 29.94$ kpc. The projected best-fit curve is overlaid in Figure 9(a).

Figure 9(b) shows a three-dimensional stellar mass density profile, $\rho_s(r) = \Upsilon_0 j(r)$, derived with an R -band mass-to-light ratio of $\Upsilon_0 = 6.5 M_\odot L_{R,\odot}^{-1}$ (determined in the next section). From this profile, we obtain an M86 stellar mass profile represented by

$$M_s(r) = \int_0^r 4\pi x^2 \rho_s(r) dx = \Upsilon_0 \int_0^r 4\pi x^2 j(x) dx$$

$$= \Upsilon_0 L_{\text{tot}} \left[\frac{(r/a)^{1/2}}{1 + (r/a)^{1/2}} \right]^{2(3-\gamma)} \left[\frac{(7-2\gamma) + (r/a)^{1/2}}{1 + (r/a)^{1/2}} \right]. \quad (7)$$

4.3.3. Extended Dark Matter Halo in M86

If we adopt the stellar mass profile as the total mass profile (i.e., $M_{\text{tot}}(r) = M_s(r)$) and $\rho_s(r) \propto j(r)$ instead of $n_{\text{cl}}(r)$, we can derive the radial component of VDPs for the stellar system from the Jeans equation. We also assume R -band mass-to-light ratios (Υ_0) and velocity anisotropies of the stellar halo ($\beta_s(r)$). The projected VDPs are then computed from the radial component of VDPs through Equation (3).

Figure 10 plots the M86 GC VDP measured in this study and the observed M86 stellar VDP given in Bender et al. (1994). The stellar velocity dispersion is almost constant around 220 km s^{-1} in the inner region and is smoothly connected to the GC velocity dispersion at $R \approx 3$ kpc. We also plot the predicted VDPs derived with $\Upsilon_0 = 5.0 M_\odot L_{R,\odot}^{-1}$, $\beta_s(r) = 0.4$ (radially biased) and $\Upsilon_0 = 6.5 M_\odot L_{R,\odot}^{-1}$, $\beta_s(r) = 0.0$ (isotropic), which fit the observed stellar kinematic data at $R < 2$ kpc well. For

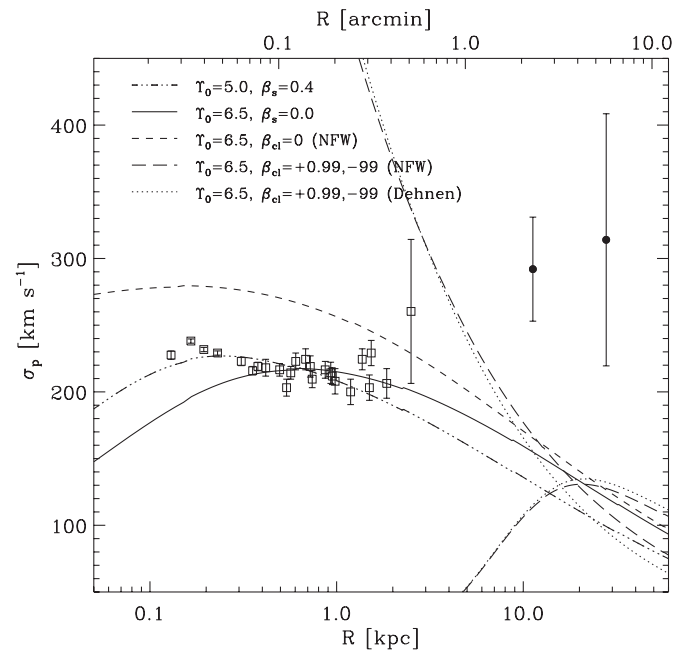


Figure 10. VDPs for the stars and GCs in M86. The open squares represent the stellar velocity dispersions from Bender et al. (1994). The filled circles show the velocity dispersions of the GCs. The solid line represents the stellar VDP expected from the stellar mass model with a constant stellar mass-to-light ratio of $\Upsilon_0 = 6.5 M_\odot L_{R,\odot}^{-1}$ and a stellar velocity anisotropy of $\beta_s = 0.0$. The triple-dot-dashed curve shows the stellar VDP with $\Upsilon_0 = 5.0 M_\odot L_{R,\odot}^{-1}$ and $\beta_s = 0.4$. Also shown are VDPs expected from the same stellar mass model as above but with NFW GC density profiles and velocity anisotropies of $\beta_{\text{cl}} = 0.0$ (short dashed line) and $+0.99, -99$ (long dashed lines). The dotted lines represent the VDPs with a Dehnen density profile at $\beta_{\text{cl}} = +0.99$ and -99 .

comparison, the predicted VDPs for the M86 GCs derived with the same stellar mass profile, the GC number density profiles ($n_{\text{cl}}^{\text{NFW}}(r)$ and $n_{\text{cl}}^{\text{Dehnen}}(r)$) determined in the previous section, and several velocity anisotropies ($\beta_{\text{cl}}(r) = +0.99$ (radially biased), 0.0 (isotropic), and -0.99 (tangentially biased)) are also shown. The VDPs based on the NFW and Dehnen density profiles are not significantly different from each other. Note that none of the models agree with the observed VDPs of the GCs at $R > 3$ kpc, which suggests that the mass-to-light ratio is not constant over the galactocentric radius but should increase with the radius. This clearly suggests the existence of an extended dark matter halo in the outer region of M86.

5. METALLICITIES AND AGES

5.1. Metallicity and Age Measurement

We determined the metallicities and ages of the M86 GCs using two methods: (1) the BH method, which determines the metallicity through an empirical relation between the absorption line index and metallicity developed by Brodie & Huchra (1990), and (2) the grid method, which derives metallicity and age from a comparison of the Lick line index of the spectrum with that of a single stellar population (SSP) model. We explain each method here.

5.1.1. BH Method

Brodie & Huchra (1990) and Huchra et al. (1996) presented linear relations between absorption line indices obtained from the integrated spectra and mean metallicities to derive the metal abundances of old stellar systems. Their method was developed to minimize systematic effects such as reddening, individual element abundance anomalies, and instrumental effects. They recommend six indices (G band, MgH, Mg2, Fe5270, CNB, and Δ) as primary calibrators among the 12 line indices for the empirical relations. Here, we use only four primary line indices to determine the metallicities of the M86 GCs (G band, MgH, Mg2, and Fe5270) because of the low S/N of the spectra in the wavelength range for the CNB and Δ indices.

Each spectrum is first shifted into the rest frame, and we then measure the absorption line indices following the prescription of Brodie & Huchra (1990) and Huchra et al. (1996). The measured absorption line indices are calibrated to the BH index system with a zero-point offset, $\text{Index (BH)} = \text{Index (Subaru)} + \text{offset}$, determined from the indices of five MW GCs that are common to this study and Huchra et al. (1996). The offsets we derived are 0.014 ± 0.015 for the G band, -0.013 ± 0.009 for MgH, -0.021 ± 0.018 for Mg2, and 0.008 ± 0.009 for Fe5270. We determine the metallicity from each index as follows: $[\text{Fe}/\text{H}]_{G \text{ band}} = 11.415 \times G \text{ band} - 2.455$, $[\text{Fe}/\text{H}]_{\text{MgH}} = 20.578 \times \text{MgH} - 1.840$, $[\text{Fe}/\text{H}]_{\text{Mg2}} = 9.921 \times \text{Mg2} - 2.212$, and $[\text{Fe}/\text{H}]_{\text{Fe5270}} = 20.367 \times \text{Fe5270} - 2.086$. Finally, we take an error-weighted average of the four measurements as the final metallicity value for each GC. Here, the error is the mean of the standard deviation. We are able to determine the metallicity for 16 of 25 GCs based on this method. The metallicities for the other nine GCs could not be determined because of the low S/N of the spectra.

5.1.2. Lick Index Grid Method

Lick absorption line indices are useful for determining the metallicity and age of old stellar systems by comparing the indices derived from the spectra with the line index grids

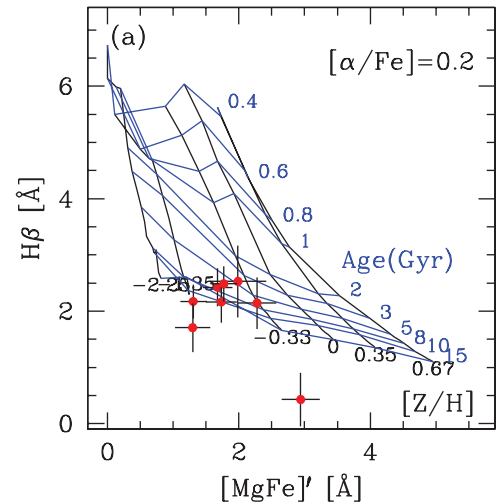


Figure 11. $H\beta$ vs. $[\text{MgFe}]'$ for the M86 GCs. The grids represent the SSP models with $[\alpha/\text{Fe}] = 0.2$ for various values of $[\text{Z}/\text{H}]$ (-2.25 , -1.35 , -0.33 , 0 , 0.35 , and 0.67) and ages (0.4–15 Gyr) given by Thomas et al. (2003).

(A color version of this figure is available in the online journal.)

predicted from SSP models (Tripicco & Bell 1995; Trager et al. 2000, 2008; Thomas et al. 2004; Puzia et al. 2005; Beasley et al. 2008; Woodley et al. 2010). For this grid method, we adopt the SSP models given by Thomas et al. (2003, 2004, 2005) and follow the technique described in Puzia et al. (2005) and Park et al. (2012).

We calibrate our absorption line indices to the Lick index system as follows. The spectra are smoothed with the Lick resolution (Worthey & Ottaviani 1997) after shifting each spectrum into the rest frame. Lick line indices are then derived from the spectra of the M86 GCs, following the definitions given in Worthey (1994) and Worthey & Ottaviani (1997). Here, the line index errors are derived from the photon noise in the spectra before the flux calibration. The resulting line indices are then calibrated to the Lick system with the zero-point offset, $\text{Index (Lick)} = \text{Index (Subaru)} + \text{offset}$, determined from the spectra of five MW GCs that are common to this study, Trager et al. (1998), and Kuntschner et al. (2002). The offsets we derived are 0.184 ± 0.140 for $H\beta$, 0.165 ± 0.187 for Mg b, 0.443 ± 0.306 for Fe5270, and -0.103 ± 0.162 for Fe5335 (see Table 1 in Park et al. (2012) for the offsets of other indices). We determined the Lick line indices for eight GCs in M86, which are listed with errors in Table 5.

The composite index $[\text{MgFe}]'$, defined by $[\text{MgFe}]' = \sqrt{\text{Mg b} \times (0.72 \times \text{Fe5270} + 0.28 \times \text{Fe5335})}$, is a good metallicity tracer because of its low sensitivity to $[\alpha/\text{Fe}]$. The index $H\beta$ is an age indicator and the least sensitive to $[\alpha/\text{Fe}]$ among the Balmer lines (Thomas et al. 2003). Thus, we determine the metallicity and age of each GC in the $H\beta$ versus $[\text{MgFe}]'$ grids provided by Thomas et al. (2003). Figure 11 shows the observational indices of the M86 GCs in comparison with the SSP model grids for $H\beta$ versus $[\text{MgFe}]'$, which indicate SSP models with $[\alpha/\text{Fe}] = 0.2$, $[\text{Z}/\text{H}] = -2.25$, -1.35 , -0.33 , 0 , 0.35 , and 0.67 dex, and ages of 0.4, 0.6, 0.8, 1, 2, 3, 5, 8, 10, and 15 Gyr. All the GCs seem to be older than ~ 5 Gyr and metallicities smaller than the solar abundance. For the GCs inside the envelope of the model grid, we take the $[\text{Z}/\text{H}]$ value and age at the nearest model grid interpolated with bins of 0.01 dex for $[\text{Z}/\text{H}]$ and 0.1 Gyr for age. For the GCs outside the envelope, we take the values of the nearest envelope of the model grid in

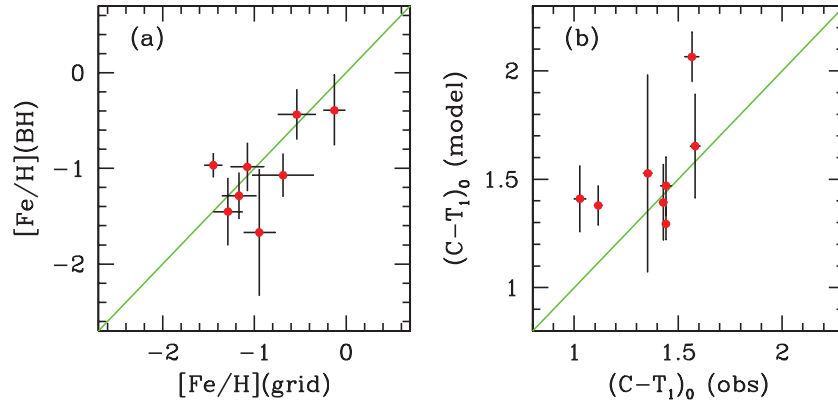


Figure 12. (a) Comparison of the M86 GC metallicities measured using the BH and grid methods. (b) Comparison of the photometric colors obtained from the observation and a model. $(C - T_1)_0$ (obs) are the observational colors from Park (2012) and $(C - T_1)_0$ (model) are the model colors derived from the $[Z/H]$ and age of the M86 GCs using the SSP model of Marigo et al. (2008). The solid lines represent one-to-one relations.

(A color version of this figure is available in the online journal.)

Table 5
Lick Line Indices and Errors

ID	H β (\AA)	Mg2 (mag)	Mgb (\AA)	Fe5270 (\AA)	Fe5335 (\AA)
65	2.423 ± 0.340	0.120 ± 0.006	2.765 ± 0.340	0.996 ± 0.359	1.074 ± 0.459
270	2.527 ± 0.641	0.075 ± 0.012	3.316 ± 0.623	2.496 ± 0.659	-2.172 ± 0.909
107	2.142 ± 0.458	0.179 ± 0.008	3.635 ± 0.444	2.037 ± 0.457	-0.147 ± 0.602
143	0.427 ± 0.474	0.102 ± 0.008	3.255 ± 0.448	2.762 ± 0.478	2.387 ± 0.574
58	2.173 ± 0.301	0.109 ± 0.005	0.814 ± 0.307	2.114 ± 0.312	2.031 ± 0.399
79	2.164 ± 0.368	0.072 ± 0.007	0.916 ± 0.363	2.585 ± 0.380	5.069 ± 0.475
96	2.487 ± 0.312	-0.005 ± 0.006	1.128 ± 0.314	3.116 ± 0.319	1.920 ± 0.420
149	1.705 ± 0.432	0.043 ± 0.007	1.164 ± 0.404	1.955 ± 0.430	0.134 ± 0.556

the direction of the error vector as done in Puzia et al. (2005). The two outliers with a large difference from the model envelope along the H β axis might be due to a limit of the low-resolution-integrated spectroscopy or of the model grids because these objects are also often shown in studies of MW GCs and M31 GCs derived from high S/N spectra (Puzia et al. 2002, 2005; Schiavon et al. 2012) as well as other gE GCs (Cenarro et al. 2007; Woodley et al. 2010). To estimate the errors in the age and metallicity, we calculate the ages and metallicities of four data points composed of H β \pm error and $[\text{MgFe}]' \pm$ error in the grid. The difference between the average of these four values and the estimate calculated directly from the *index* is taken as the final error.

The metallicities of eight GCs derived from the grid method are compared with those from the BH method in Figure 12(a). The two measurements are broadly consistent within the uncertainty. Here, the total metallicity ($[Z/H]$) derived from the grid method was converted into $[\text{Fe}/H](\text{grid})$ using the relation $[\text{Fe}/H] = [Z/H] - 0.94 [\alpha/\text{Fe}]$ (Thomas et al. 2003). For this conversion, we adopted $[\alpha/\text{Fe}] = 0.2$, which is the mean $[\alpha/\text{Fe}]$ for the GCs in gEs (Park et al. 2012). We also compared the observational $(C - T_1)_0$ colors of the M86 GCs (Park 2012) with the model colors derived from the $[Z/H]$ and age using the SSP model in Marigo et al. (2008). Among the eight GCs, five GCs agree well within their errors as shown in Figure 12(b).

5.2. Metallicities and Ages of the M86 GCs

The metallicities and ages of the M86 GCs are listed in Table 3, and Figure 13 shows (1) $[\text{Fe}/H]$ versus R , (2) age versus R , (3) $[\text{Fe}/H]$ distribution, and (4) age distribution of the M86 GCs. It is not easy to derive any systematic trend in the data

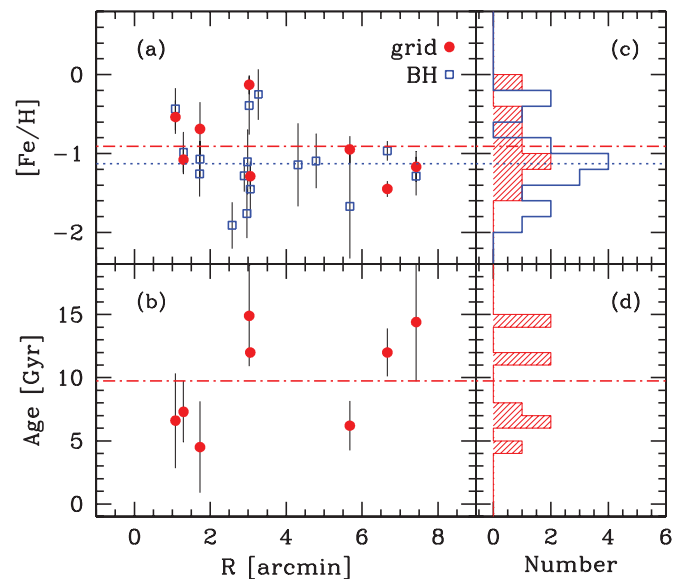


Figure 13. Metallicities and ages of the M86 GCs as a function of galactocentric radii and their histograms. The filled circles and hatched histograms indicate the values from the grid method, while the open squares and solid histogram are those from the BH method. The horizontal dot-dashed and dotted lines indicate the mean values of each parameter measured from the grid and BH methods, respectively.

(A color version of this figure is available in the online journal.)

because of small number statistics. However, several features are noted. First, the metallicities of the 16 GCs based on the BH method show a wide range of $-2.0 < [\text{Fe}/H] < -0.2$ with a mean value of -1.13 ± 0.47 , which is similar to that based

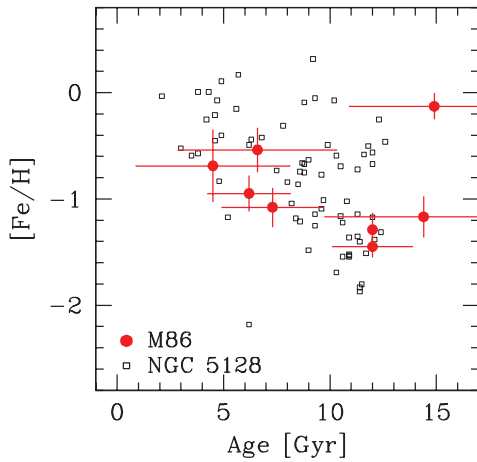


Figure 14. Age vs. metallicity of the GCs in M86. The circles and squares represent the GCs of M86 and NGC 5128, respectively.

(A color version of this figure is available in the online journal.)

on the grid method (-0.91 ± 0.44). Second, metal-rich GCs ($[\text{Fe}/\text{H}] > -0.9$) are found only in the inner region ($R \leq 4'$). Third, the age of the M86 GCs also shows a wide range from 4 to 15 Gyr with a mean of 9.7 ± 4.0 Gyr. This is similar to the GCs in other gEs (e.g., Woodley et al. 2010; Park et al. 2012).

Figure 14 shows the metallicity as a function of age for the M86 GCs. This figure hints at an age–metallicity relation, meaning that the younger GCs are more metal-rich. This relationship in gEs has also been seen for the GCs in M60 (Pierce et al. 2006) and in NGC 5128 (Woodley et al. 2010). However, Woodley et al. (2010) did not strongly confirm its existence because of large biases in their selected GC sample (e.g., extremely bright clusters). A more complete analysis with a more comprehensive data set of gE GCs is necessary to draw a strong conclusion about the age–metallicity relation.

6. SUMMARY

Using the Subaru spectroscopic data of M86 GCs, we studied the kinematic and chemical properties of the M86 GC system. Our main results are summarized as follows.

1. For the first time, we measured the radial velocities of 31 objects in the M86 field: 25 M86 GCs, 2 foreground stars, 1 probable intracluster GC in the Virgo Cluster, 2 faint galaxies, and the M86 nucleus.
2. The mean velocity of the GCs is $\overline{v_p} = -354_{-79}^{+81}$ km s $^{-1}$, which is different from the velocity of the M86 nucleus ($v_{\text{gal}} = -234 \pm 41$ km s $^{-1}$). The velocity dispersion of the GCs is $\sigma_p = 292_{-32}^{+32}$ km s $^{-1}$. The M86 GC system shows a hint of rotation.
3. From a comparison of the VDPs predicted from the stellar mass profile with the observed VDPs of the stars and GCs, we found evidence for the existence of an extended dark matter halo in M86.
4. We determined the metallicities for 16 GCs using the BH method, and the ages and metallicities for 8 GCs using the grid method. The metallicity of the M86 GCs derived from the BH method is in the range of $-2.0 < [\text{Fe}/\text{H}] < -0.2$ with a mean value of -1.13 ± 0.47 . The grid method results in similar $[\text{Fe}/\text{H}]$ values and a mean age of 9.7 ± 4.0 Gyr.

The authors thank the anonymous referee for his/her useful comments that improved the original manuscript. The authors are grateful to the staff of the Subaru telescope for their kind help

during the observation and to our collaborator Nobuo Arimoto. This work is supported in part by Mid-career Researcher Program through an NRF grant funded by MEST (No. 2010-0013875). H.S.H. acknowledges the support of the Smithsonian Institution.

REFERENCES

- Beasley, M. A., Bridges, T., Peng, E. W., et al. 2008, *MNRAS*, **386**, 1443
- Beasley, M. A., Sharples, R. M., Bridges, T. J., et al. 2000, *MNRAS*, **318**, 1249
- Beers, T. C., Flynn, K., & Gebhardt, K. 1990, *AJ*, **100**, 32
- Bender, R., Saglia, R. P., & Gerhard, O. E. 1994, *MNRAS*, **269**, 785
- Beuing, J., Dobreiner, S., Bohringer, H., & Bender, R. 1999, *MNRAS*, **302**, 209
- Binney, J., & Tremaine, S. 1987, *Galactic Dynamics* (Princeton, NJ: Princeton Univ. Press)
- Bridges, T., Gebhardt, K., Sharples, R., et al. 2006, *MNRAS*, **373**, 157
- Brodie, J. P., & Huchra, J. P. 1990, *ApJ*, **362**, 503 (BH)
- Brodie, J. P., & Strader, J. 2006, *ARA&A*, **44**, 193
- Caon, N., Capaccioli, M., & Rampazzo, R. 1990, *A&AS*, **86**, 429
- Cenarro, A. J., Beasley, M. A., Strader, J., Brodie, J. P., & Forbes, D. A. 2007, *AJ*, **134**, 391
- Chakrabarty, D., & Raychaudhury, S. 2008, *AJ*, **135**, 2350
- Cohen, J. G., Blakeslee, J. P., & Côté, P. 2003, *ApJ*, **592**, 866
- Cohen, J. G., Blakeslee, J. P., & Ryzhov, A. 1998, *ApJ*, **496**, 808
- Cohen, J. G., & Ryzhov, A. 1997, *ApJ*, **486**, 230
- Côté, P., McLaughlin, D. E., Cohen, J. G., & Blakeslee, J. P. 2003, *ApJ*, **591**, 850
- Côté, P., McLaughlin, D. E., Hanes, D. A., et al. 2001, *ApJ*, **559**, 828
- Dehnen, W. 1993, *MNRAS*, **265**, 250
- de Vaucouleurs, G., de Vaucouleurs, A., Corwin, H. G., Jr., et al. 1991, *Third Reference Catalog of Bright Galaxies* (New York: Springer)
- Forbes, D. A., Beasley, M. A., Brodie, J. P., & Kissler-Patig, M. 2001, *ApJ*, **563**, L143
- Huchra, J. P., Brodie, J. P., Caldwell, N., et al. 1996, *ApJS*, **102**, 29
- Hwang, H. S., Lee, M. G., Park, H. S., et al. 2008, *ApJ*, **674**, 869
- Jordán, A., Peng, E. W., Blakeslee, J. P., et al. 2009, *ApJS*, **180**, 54
- Kashikawa, N., Aoki, K., Asai, R., et al. 2002, *PASJ*, **54**, 819
- Kim, S. C., Lee, M. G., Geisler, D., et al. 2007, *AJ*, **134**, 706
- Kissler-Patig, M., Brodie, J. P., Schroder, L. L., et al. 1998, *AJ*, **115**, 105
- Kissler-Patig, M., & Gebhardt, K. 1998, *AJ*, **116**, 2237
- Kissler-Patig, M., Grillmair, C. J., Meylan, G., et al. 1999, *AJ*, **117**, 1206
- Kormendy, J., Fisher, D. B., Cornell, M. E., & Bender, R. 2009, *ApJS*, **182**, 216
- Krajinović, D., Emsellem, E., Cappellari, M., et al. 2011, *MNRAS*, **414**, 2923
- Kundu, A., & Whitmore, B. C. 2001, *AJ*, **121**, 2950
- Kuntschner, H., Ziegler, B. L., Sharples, R. M., Worthey, G., & Fricke, K. J. 2002, *A&A*, **395**, 761
- Larsen, S. S., Brodie, J. P., Huchra, J. P., Forbes, D. A., & Grillmair, C. J. 2001, *AJ*, **121**, 2974
- Lee, M. G. 2003, *J. Korean Astron. Soc.*, **36**, 189
- Lee, M. G., Hwang, H. S., Kim, S. C., et al. 2008a, *ApJ*, **674**, 886
- Lee, M. G., Hwang, H. S., Park, H. S., et al. 2008b, *ApJ*, **674**, 857
- Lee, M. G., Park, H. S., Hwang, H. S., et al. 2010a, *ApJ*, **709**, 1083
- Lee, M. G., Park, H. S., & Hwang, H. S. 2010b, *Science*, **328**, 334
- Lee, M. G., Park, H. S., Kim, E., et al. 2008c, *ApJ*, **682**, 135
- Marigo, P., Girardi, L., Bressan, A., et al. 2008, *A&A*, **482**, 883
- Mei, S., Blakeslee, J. P., Côté, P., et al. 2007, *ApJ*, **655**, 144
- Minniti, D., Kissler-Patig, M., Goudfrooij, P., & Meylan, G. 1998, *AJ*, **115**, 121
- Navarro, J. F., Frenk, C. S., & White, S. D. M. 1997, *ApJ*, **490**, 493
- Park, H. S. 2012, *J. Korean Astron. Soc.*, **45**, 71
- Park, H. S., Lee, M. G., Hwang, H. S., et al. 2010, *ApJ*, **709**, 377
- Park, H. S., Lee, M. G., Hwang, H. S., et al. 2012, *ApJ*, submitted
- Peletier, R. F., Davies, R. L., Illingworth, G. D., Davis, L. E., & Cawson, M. 1990, *AJ*, **100**, 1091
- Peng, E. W., Ford, H. C., & Freeman, K. C. 2004a, *ApJS*, **150**, 367
- Peng, E. W., Ford, H. C., & Freeman, K. C. 2004b, *ApJ*, **602**, 705
- Peng, E. W., Jordán, A., Côté, P., et al. 2006, *ApJ*, **639**, 95
- Pierce, M., Bridges, T., Forbes, D. A., et al. 2006, *MNRAS*, **368**, 325
- Puzia, T. H., Perrett, K. M., & Bridges, T. J. 2005, *A&A*, **434**, 909
- Puzia, T. H., Zepf, S. E., Kissler-Patig, M., et al. 2002, *A&A*, **391**, 453
- Rhode, K. L., & Zepf, S. E. 2004, *AJ*, **127**, 302
- Richtler, T., Dirsch, B., Gebhardt, K., et al. 2004, *AJ*, **127**, 2094
- Richtler, T., Schuberth, Y., Hilker, M., et al. 2008, *A&A*, **478**, L23
- Romanowsky, A. J., Strader, J., Spitler, L. R., et al. 2009, *AJ*, **137**, 4956
- Saito, Y., Ohya, Y., Kashikawa, N., et al. 2003, *Proc. SPIE*, **4841**, 1180

- Santos, J. F. C. J., Alloin, D., Bica, E., & Bonatto, C. 2002, in IAU Symp. 207, Extragalactic Star Clusters, ed. D. Geisler, E. K. Grebel, & D. Minniti (Cambridge: Cambridge Univ. Press), 1
- Schiavon, R. P., Caldwell, N., Morrison, H., et al. 2012, *AJ*, 143, 14
- Schuberth, Y., Richtler, T., Dirsch, B., et al. 2006, *A&A*, 459, 391
- Schuberth, Y., Richtler, T., Hilker, M., et al. 2010, *A&A*, 513, A52
- Smith, R. J., Lucey, J. R., Hudson, M. J., Schlegel, D. J., & Davies, R. L. 2000, *MNRAS*, 313, 469
- Strader, J., Romanowsky, A. J., Brodie, J. P., et al. 2011, *ApJS*, 197, 33
- Strauss, M. A., Huchra, J. P., Davis, M., et al. 1992, *ApJS*, 83, 29
- Teague, P. F., Carter, D., & Gray, P. M. 1990, *ApJS*, 72, 715
- Thomas, D., Maraston, C., & Bender, R. 2003, *MNRAS*, 339, 897
- Thomas, D., Maraston, C., Bender, R., & Mendes de Oliveira, C. 2005, *ApJ*, 621, 673
- Thomas, D., Maraston, C., & Korn, A. 2004, *MNRAS*, 351, L19
- Tonry, J., & Davis, M. 1979, *AJ*, 84, 1511
- Trager, S. C., Faber, S. M., & Dressler, A. 2008, *MNRAS*, 386, 715
- Trager, S. C., Faber, S. M., Worthey, G., & González, J. J. 2000, *AJ*, 119, 1645
- Trager, S. C., Worthey, G., Faber, S. M., Burstein, D., & Gonzalez, J. J. 1998, *ApJS*, 116, 1
- Tripicco, M., & Bell, R. A. 1995, *AJ*, 110, 3035
- Woodley, K. A., & Gómez, M. 2010, *PASA*, 27, 379
- Woodley, K. A., Harris, W. E., Beasley, M. A., et al. 2007, *AJ*, 134, 494
- Woodley, K. A., Harris, W. E., Puzia, T. H., et al. 2010, *ApJ*, 708, 1335
- Worthey, G. 1994, *ApJS*, 95, 107
- Worthey, G., & Ottaviani, D. L. 1997, *ApJS*, 111, 377
- Zepf, S. E., Beasley, M. A., Bridges, T. J., et al. 2000, *AJ*, 120, 2928